Wireless Magnetic Actuation with a Bistable Parity-Time-Symmetric Circuit

Zhenya Dong,[1] Han-Joon Kim,[1,2] Hongjian Cui,[1] Chenhui Li,[1] Cheng-Wei Qiu,[1] and John S. Ho[1,2,3,*]

[1] *Department of Electrical and Computer Engineering, National University of Singapore, Singapore 117583, Singapore*

[2] *Institute for Health Innovation and Technology, National University of Singapore, Singapore 117599, Singapore*

[3] *The N.1 Institute for Health, National University of Singapore, Singapore 117456, Singapore*

Magnetic forces in oscillating electronic circuits provide a versatile way to remotely actuate objects. However, practical control of these forces is challenging due to variations in the circuit configuration and noise. We show that these challenges can be overcome using a bistable parity-time-symmetric circuit. Due to nonlinear parity-time symmetry, the circuit automatically tracks one of two eigenmodes corresponding to resonant attraction and repulsion during variations in the operating configuration. We show that noise facilitates controllable switching between the modes, and experimentally demonstrate practical actuation by remotely driving a pendulum and a soft pump membrane.

I. INTRODUCTION

Wireless actuation of objects with magnetic fields has important technological applications ranging from controlled drug delivery to robotic propulsion [1–9]. Typically, the actuating force is generated by interaction with a magnetized object, but challenges in materials processing and interoperability with other technologies, such as magnetic resonance imaging, motivate schemes that do not require the use of magnetic materials [10,11]. Magnetic forces in oscillating electronic circuits provide a versatile alternative approach to realize wireless actuation. The standard setup comprises two inductively coupled coils, corresponding to the actuator and the object, that experience an attractive or repulsive force depending on the phase between the currents flowing through the coils [12–14]. The actuating force is set by tuning the object to resonance and carefully adjusting the driving frequency of the actuator near the resonance to obtain the desired phase. However, practical control of the actuating force is challenging because of intrinsic system noise and variations in the coupling strength during actuation.

Concepts in wireless power transfer relate to the design of wireless actuation systems because of their close similarities in terms of the circuit setup [15,16]. Recently, motivated by the application of concepts in non-Hermitian physics to photonics, acoustics, and electronics [17–26], parity-time ($\mathcal{PT}$)-symmetric arrangements of resonant circuits have been shown to provide wireless power transfer that is robust to variations in the operating conditions [27–30]. In this scheme, energy is injected into the source resonator through a nonlinear gain element instead of a fixed-frequency signal. This circuit self-oscillates at a frequency corresponding to one of the eigenmodes of the $\mathcal{PT}$-symmetric system, and automatically tracks this frequency to provide constant power transfer across a large range of separation distances. Due to the existence of multiple eigenmodes, previous studies have observed spontaneous mode transitions that result in abrupt changes in the oscillation frequency and reversal of the sign of the phase between source and receiver [27]. These transitions have thus far been largely ignored because they have a negligible effect on the power transfer efficiency, but are important to wireless actuation because they result in switching between attraction and repulsion. Understanding and controlling these mode transitions are essential for fully harnessing the unique properties of $\mathcal{PT}$-symmetric systems for actuation and other technological applications.

In this paper, we study the mechanisms underlying mode transitions in nonlinear $\mathcal{PT}$-symmetric circuits, and show that they enable practical control of wireless actuation. We investigate the role of noise and show that mode transitions can be controllably induced by detuning beyond the threshold. Analogous to $\mathcal{PT}$-symmetric circuits for robust wireless power transfer, the wireless actuation circuit maintains the optimal magnetic force on the object even during movement. In contrast with prior designs, however, the system is capable of rapidly and controllably switching between oscillating modes corresponding to attraction and

*johnho@nus.edu.sg

024023-1

repulsion. Using this approach, we demonstrate wireless actuation of a pendulum and a soft pump membrane.

II. THEORY

A. $\mathcal{PT}$-symmetric actuation system

Figure 1(a) shows the system configuration consisting of the actuator circuit inductively coupled to the object circuit with coupling rate κ. The amplitudes of the currents flowing through the actuator and object are, respectively, normalized to a_1 and a_2 such that $|a_n|^2$ corresponds to the magnetic energy in each coil. Assuming that the circuit oscillates at frequency ω, the time-averaged magnetic force between the actuator and the object is given by

$$F = \frac{8\pi}{\omega} \frac{\partial \kappa}{\partial z_Q} |a_1||a_2| \cos\phi, \tag{1}$$

where z_Q is the distance between the coils and ϕ the phase between a_1 and a_2 [31]. In contrast to wireless power transfer where ϕ has negligible effect on efficiency, the phase ϕ plays a critical role in actuation because it determines the direction and amplitude of the force.

Following previous analyses of this circuit for wireless power transfer [15,16,27,29,32], we describe the dynamics of a_1 and a_2 using coupled-mode theory. The object has a resonant frequency ω_0 and an intrinsic loss rate γ_2, while the actuator has a detuned resonant frequency $\omega_0 + \varepsilon$ and a loss rate γ_1. The system dynamics are described by

$$\begin{pmatrix} \dot{a}_1 \\ \dot{a}_2 \end{pmatrix} = \begin{pmatrix} i(\omega_0 + \varepsilon) - \gamma_1 & -i\kappa \\ -i\kappa & i\omega_0 - \gamma_2 \end{pmatrix} \begin{pmatrix} a_1 \\ a_2 \end{pmatrix}. \tag{2}$$

Assuming a time dependency of $e^{i\omega t}$, the eigenfrequencies $\omega_\pm$ can be determined by solving the characteristic equation in the variable ω [27,33,34]. For the zero detuning $\varepsilon = 0$, the two eigenfrequencies are given by

$$\omega_\pm = \omega_0 \pm \frac{1}{2}\sqrt{4\kappa^2 - (\gamma_1 - \gamma_2)^2} + \frac{1}{2}i(\gamma_1 + \gamma_2). \tag{3}$$

The steady-state behavior of the system can be understood by considering the real and imaginary parts of $\omega_\pm$ as a function of γ_1, as shown in Fig. 1(b). In both the standard wireless power transfer and wireless actuation schemes, the actuating circuit is intrinsically lossy, $\gamma_1 > 0$. For such systems, the corresponding eigenfrequencies are strictly decaying with the growth rate $-\text{Im}\{\omega_\pm\} < 0$, and an external driving signal is required to inject energy into the system and sustain an oscillation at an arbitrary frequency ω in the steady state. Furthermore, the systems are typically operated near $\gamma_1 = \gamma_2$ in order to maximize power transfer to the object. In this case, $\text{Re}\{\omega_\pm\}$ vary as a function of κ, which implies that the optimal driving frequency is sensitive to object movement.
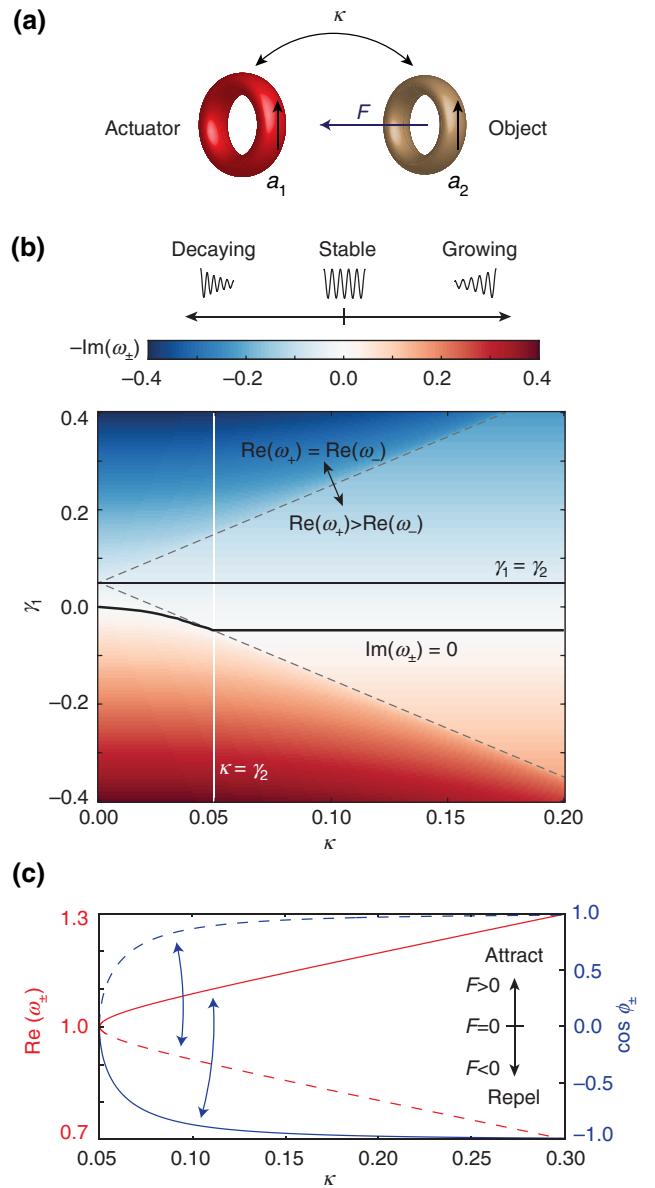

(a)

(b)

(c)

FIG. 1. Wireless actuation system. (a) Setup consisting of the actuator and object resonators with current amplitudes a_n, coupling rate κ, and force F. (b) Topology of the imaginary parts of the eigenfrequencies $-\text{Im}(\omega_\pm)$ as a function of γ_1 and κ. Introducing gain $\gamma_1 < 0$ provides access to stable solutions $\text{Im}(\omega_\pm) = 0$ (thick black line). (c) Real parts of the eigenfrequencies $\text{Re}(\omega_\pm)$ and phase $\cos\phi_\pm$ for the stable solutions. The solid curves correspond to the mode ω_+ while the dashed ones correspond to the other mode ω_-. Parameters are $\omega_0 = 1$, $\gamma_2 = 0.05$, and $\varepsilon = 0$.

In contrast, the $\mathcal{PT}$-symmetric approach uses an actuator (source) circuit with intrinsic gain $\gamma_1 < 0$. Figure 1(b) shows that the gain provides access to stable modes $\text{Im}\{\omega_\pm\} = 0$ that oscillate without any external driving signal via injection of energy into the system by the gain element. In this case, the oscillation frequency

ω automatically settles to one of the eigenmodes with frequency $\text{Re}\{\omega_{\pm}\}$ in the steady state. These stable solutions correspond to the condition $\gamma_1 = -\gamma_2$, where the system described by Eq. (2) satisfies $\mathcal{PT}$ symmetry. In practical implementations, this condition is satisfied by exploiting the nonlinearity of the gain element [27]. Specifically, the initial gain is set as $\gamma_1 < -\gamma_2$ such that the oscillating modes compete to grow and saturate out the gain, resulting in a single mode surviving in the steady state that has a saturated gain exactly balancing the loss.

The actuating force generated by the circuit depends critically on the phase ϕ. From Eq. (2), the eigenmodes of the system corresponding to $\omega_{\pm}$ are given by

$$\mathbf{a}_{\pm} = \begin{pmatrix} \dfrac{\mp\sqrt{4\kappa^2 - (\gamma_1 - \gamma_2)^2} - i(\gamma_1 - \gamma_2)}{2\kappa} \\ 1 \end{pmatrix}. \quad (4)$$

The system behavior is divided into two regimes depending on the coupling strength κ. In the weak coupling regime $\kappa < |\gamma_1 - \gamma_2|/2$, the phase is $\cos\phi_{\pm} = 0$ and the force on the object is zero. In the strong coupling regime $\kappa > |\gamma_1 - \gamma_2|/2$, the phase is given by $\cos\phi_{\pm} = \mp\sqrt{1 - (\gamma_1 - \gamma_2)^2/4\kappa^2}$, which rapidly approaches $\cos\phi_{\pm} = \mp 1$ as the coupling increases [Fig. 1(c)]. Here, the eigenmodes result in two possible oscillation frequencies: $\text{Re}\{\omega_+\}$, which corresponds to attraction of the object; and $\text{Re}\{\omega_-\}$, which corresponds to repulsion of the object. To provide actuation, the circuit needs to be controlled in a way that allows the oscillation mode to be selected and switched at will.

B. Noise-assisted mode transitions

We study transitions between the modes using mode competition theory, which is widely used to describe optical and microwave oscillators [35–38]. Specifically, we
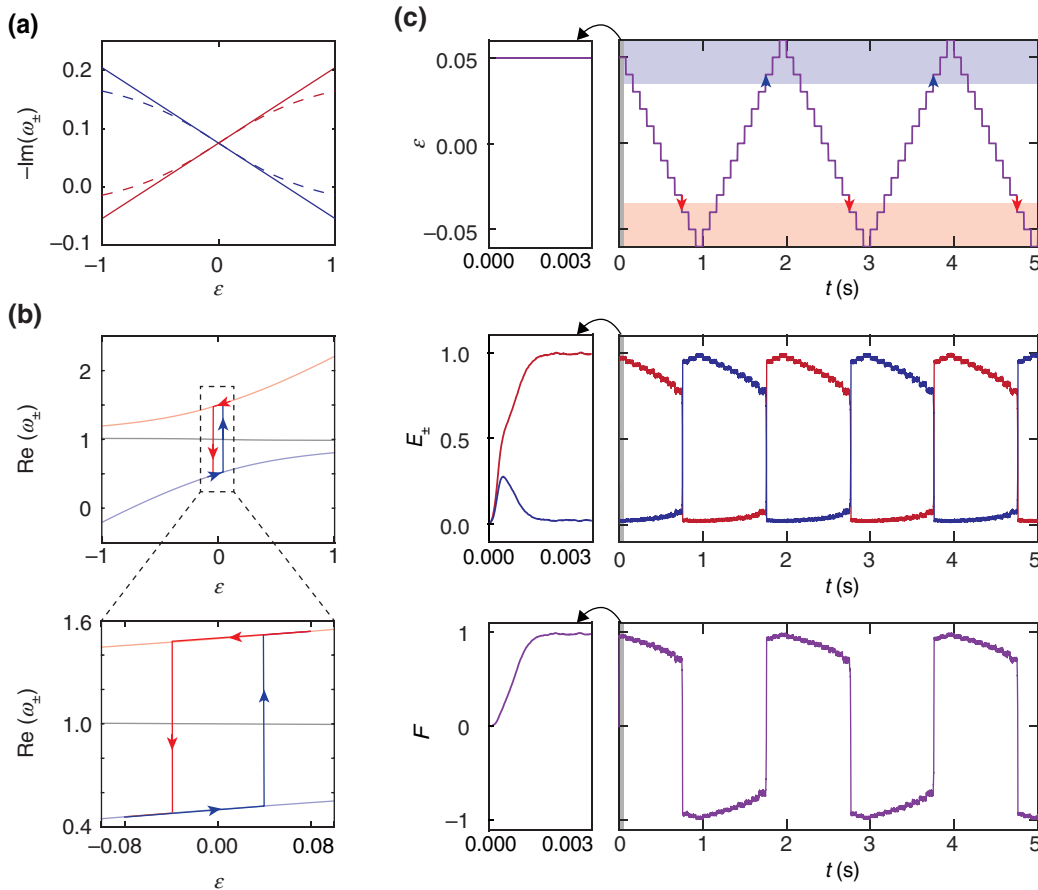

FIG. 2. Controllable mode transitions in the bistable $\mathcal{PT}$-symmetric circuit. (a) Growth rate $-\text{Im}(\omega_{\pm})$ of the eigenmodes as a function of detuning ε. Solid lines show the theoretical approximations and the dashed lines numerical solutions of the exact equations. (b) Mode transitions as ε increases and decreases for $\kappa = 0.5$. Red and blue lines denote steady-state oscillating solutions, and the gray solid line an inaccessible solution. The inset shows an enlarged view of the bistable region. (c) Ramped tuning of ε over 1-s intervals and corresponding mode energy $E_{\pm}$ and force F. Left-hand plots show the transient dynamics when the circuit is turned on. The system parameters are $\alpha = 0.001$, $\beta = 1.333 \times 10^{-3}$, $\gamma_1 = -0.2$, and $\gamma_2 = 0.05$, and the noise power is set to be 4% of the power generated by the gain element.

study the evolution of the system response considering the effects of nonzero detuning $\varepsilon \neq 0$. The detuned eigenfrequencies can be approximated as [34]

$$\omega_\pm \approx \omega_0 \pm \frac{A}{2} + \frac{1}{2}\varepsilon + \frac{1}{2}i\left(\gamma_1 + \gamma_2 \mp \frac{\gamma_2 - \gamma_1}{A}\varepsilon\right), \quad (5)$$

where $A = \sqrt{4\kappa^2 - (\gamma_1 - \gamma_2)^2}$. By setting the gain as $\gamma_1 < -\gamma_2$, the system has two eigenmodes with the growth rate $-\text{Im}(\omega_\pm) = -[\gamma_1 + \gamma_2 \mp (\gamma_2 - \gamma_1)\varepsilon/A]/2$, as shown by the solid lines in Fig. 2(a). The detuning ε biases one of the modes at a higher growth rate, which leads to the selection of a single mode due to competition for gain. To show this, we describe the evolution of the mode energies during competition in the presence of noise [39–42]. Taking $E_+ = |\mathbf{a}_+|^2$ and $E_- = |\mathbf{a}_-|^2$ to be the slowly varying energy of the two eigenmodes and $N_\pm$ to be the noise power in each mode, we have

$$\frac{dE_\pm}{dt} = E_\pm\left(\tilde{g}_\pm - \gamma_2 \pm \frac{\gamma_2 - \gamma_1}{A}\varepsilon\right) + N_\pm, \quad (6)$$

where $\tilde{g}_\pm = -\gamma_1 - \alpha E_\pm - \beta E_\mp$ is the saturable gain, with α the self-saturation and β the cross-saturation parameters of the amplifier. Equation (6) shows that detuning $\varepsilon > 0$ provides a larger growth rate for E_+, whereas $\varepsilon < 0$ biases the growth rate of E_-. The ratio β/α determines how many modes can be maintained in the steady state where $dE_\pm/dt = 0$. In the case $\beta/\alpha > 1$, the two modes will compete against each other and only one survives in the steady

state, which results in bistability, whereas both modes can coexist for $\beta/\alpha < 1$ [39,40].

We now solve for the detuning ε necessary for noise to induce transitions between the modes. We consider the case where the system is oscillating at the mode E_+, and all the noise is present in the other mode $N_+ = 0$ and $N_- = N_{\max}$. In this case, the following conditions must be satisfied to prevent the mode transition $E_+ \rightarrow E_-$ from occurring:

$$\left.\frac{dE_+}{dt}\right|_{N_+=0} = 0, \quad \left.\frac{dE_-}{dt}\right|_{N_-=N_{\max}} = 0, \quad E_\pm \neq 0. \quad (7)$$

Searching for the values of ε for which Eq. (7) does not admit solutions with real-valued $E_\pm$, the detuning required to enable mode transitions is found to be

$$\varepsilon < \frac{A(\beta - \alpha)(\gamma_1 + \gamma_2) + \sqrt{N_{\max}4\alpha A^2(\beta^2 - \alpha^2)}}{(\alpha + \beta)(\gamma_2 - \gamma_1)}. \quad (8)$$

Equation (8) shows the essential role of noise in determining the detuning required to induce mode transitions. For the transition $E_- \rightarrow E_+$, the detuning should be in the opposite direction, $\varepsilon \rightarrow -\varepsilon$.

Figure 2(b) shows the evolution of the circuit oscillation as ε is tuned in opposite directions. The mode evolution exhibits a hysteresis effect and a bistable region whose width depends on the noise power [43]. Owing to the bistability, the oscillation mode is immune to noise below the transition thresholds. Dynamic simulations of the two modes as ε is varied in a stepwise manner
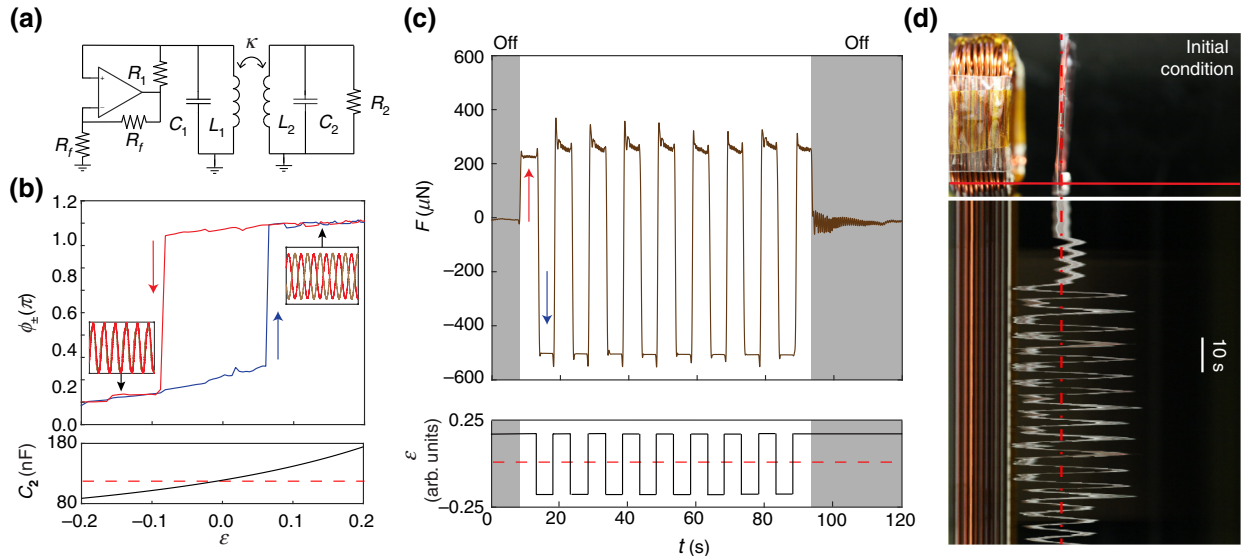

FIG. 3.　Wireless actuation circuit. (a) Schematic of the $\mathcal{PT}$-symmetric circuit. R_n is the resistance, L_n the inductance, and C_n the capacitance of the actuator (left) and object (right) circuits. The negative impedance converter has gain $-R_1$. (b) Phase ϕ as a detuning ε is varied from -0.2 to 0.2 in both directions. The bottom plot shows capacitor value C_2 corresponding to ε (normalized to $\omega_0 = 1$). (c) Force on the object in a pendulum configuration. The bottom plot shows control signal ε. (d) Image of the experimental setup (top) and pixel values along the solid red line as a function of time (bottom). Dashed red line shows initial object position.
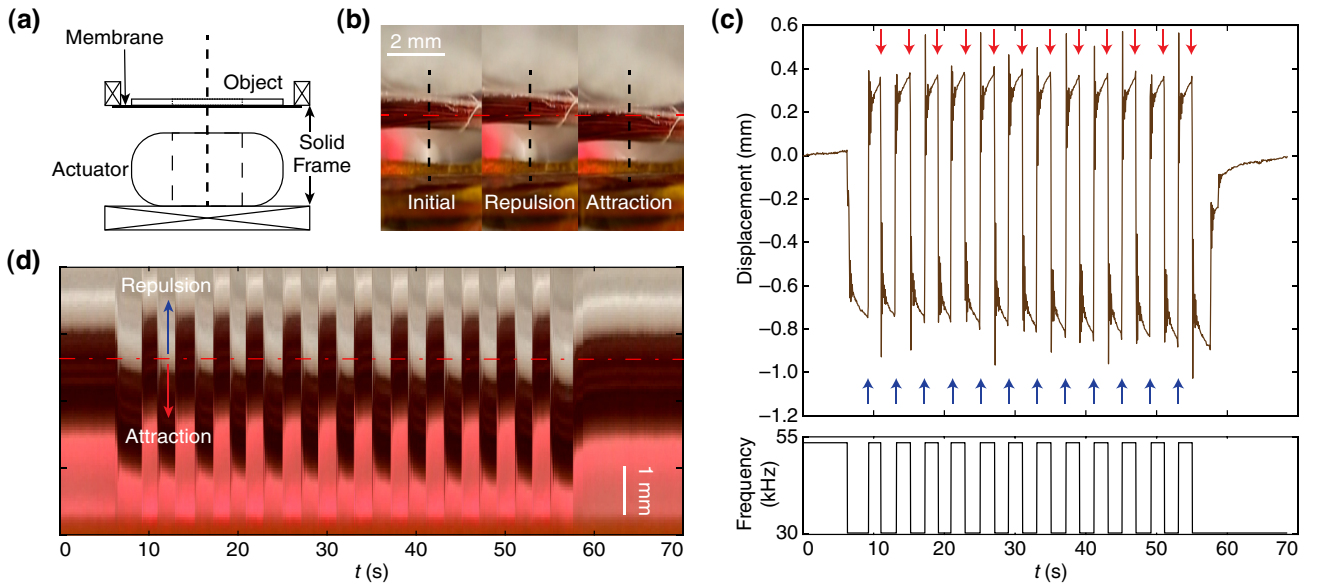
FIG. 4.   Wireless actuation of a soft pump membrane. (a) Experimental setup. (b) Images of the membrane at initial position and during repulsion and attraction. (c) Membrane displacement and oscillation frequency ω of the circuit during pulsed switching of the actuator with period of 4 s. Red arrows indicate switching to repulsion and blue arrows switching to attraction. (d) Pixel values along the black line in (b) as a function of time. Red dotted line indicates initial position.

show that switching occurs only when the detuning ε exceeds the threshold in the corresponding detuning direction [Fig. 2(c)]. These transitions result in rapid switching in the direction of the actuating force, providing a practical mechanism to control repulsion and attraction of the object.

III. EXPERIMENTAL RESULTS

We experimentally demonstrate wireless actuation using the $\mathcal{PT}$-symmetric circuit shown in Fig. 3(a). The actuating circuit comprises a copper wire inductor with a diameter of 30 mm (50 windings) with an inductance of $L_1 = 128$ μH tuned to resonance between 33.75 and 46.49 kHz using a variable capacitor. The object circuit consists of a smaller inductor (40 windings) with inductance $L_2 = 95$ μH tuned to a fixed resonance frequency of 36.5 kHz using a ceramic capacitor $C_2 = 200$ nF. The gain of the actuating circuit is realized using a negative impedance converter configured using an operational amplifier (OPA-541, Texas Instruments) with a gain rate of $\gamma_1 = -1/(2R_1C_1)$, where $R_1 = 20$ Ω. The object circuit has an intrinsic loss rate of $\gamma_2 = 1/(2R_2C_2)$ due to resistive losses in the inductor. The coupling rate between the resonant circuits is given by $\kappa = \omega M/(2\sqrt{L_1L_2})$, where M is the mutual coupling between the inductors. The mode transition behavior of the circuit is verified in Fig. 3(b), which shows the bistable region obtained when ε is varied by sweeping the variable capacitor in the range 80–180 nF.

To investigate the generated force, the object is actuated in a pendulum configuration while measuring the

displacement using a laser sensor (IL-S025, KEYENCE). The actuator switches between attractive and repulsive modes every 5 s by inducing transitions between the 53-kHz mode and the 30-kHz mode. Figure 3(c) shows that the displacement-estimated force during actuation varies between 300 and 500 μN. Visualization of the object motion shows that the actuation is repeatable and controllable over an approximately 1.5-cm range of motion despite large variations in the coupling strength [Fig. 3(d)].

We illustrate the practical utility of the wireless actuator by driving a soft pump, which is an important component in microfluidic and drug delivery devices. As shown in Fig. 4(a), the object circuit is attached to a 150-μm-thick polydimethylsiloxane membrane supported at the margins by a solid frame. The actuating circuit is placed 5 mm away from the membrane and operated with a switching period of 5 s. Figure 4(b) shows the membrane displacement in the initial state and when subject to an attractive and repulsive force. The membrane is actuated with total displacement of 1200 μm [Fig. 4(c)] with high repeatability over a duration of 60 s, demonstrating practical wireless actuation using $\mathcal{PT}$-symmetric mode transitions. The asymmetric displacement of the membrane can be attributed to the prestrain of the membrane and variation in the coupling strength during motion.

IV. CONCLUSION

We have identified the mechanisms underlying mode transitions in nonlinear $\mathcal{PT}$-symmetric systems, and demonstrated that the interplay of noise and bistability can

provide practical wireless actuation. The resulting wireless actuator automatically maintains the maximum magnetic force on the object, even during movement, and can programmably switch between attraction and repulsion of the object. The mode transition mechanisms identified here can also be generalized to higher-order $\mathcal{PT}$-symmetric systems, where mode competition results in the selection of a single mode from three or more possible modes [34]. These results are relevant to the design of wireless actuation and power transfer systems in which multiple resonators provide extended operating range, as well as wireless telemetry systems with enhanced sensitivity [30, 32,44,45]. Future work should also address approaches to increase the force generated by the actuator, which remains substantially weaker than that for magnet-based schemes owing to the low magnetization generated by induced currents. By circumventing the use of magnetic materials, this wireless actuation approach may open applications in medical devices, microfluidics, and robotics [46,47].

APPENDIX: CORRESPONDENCE WITH CIRCUIT ANALYSIS

The coupled-mode equation [Eq. (2)] can be derived from standard circuit analysis. For a pair of parallel RLC circuits coupled through mutual inductance M at frequency ω, we have

$$i\omega \begin{pmatrix} L_1 & M \\ M & L_2 \end{pmatrix} \begin{pmatrix} I_{L,1} \\ I_{L,2} \end{pmatrix} - \begin{pmatrix} V_1 \\ V_2 \end{pmatrix} = 0, \quad (A1)$$

where V_n are the voltages and $I_{L,n}$ the currents flowing through the inductors L_n. Furthermore, Kirchoff's current law requires

$$
\begin{aligned}
I_{L,1} + \frac{V_1}{R_1} + i\omega C_1 V_1 = 0, \\
I_{L,2} + \frac{V_2}{R_2} + i\omega C_2 V_2 = 0,
\end{aligned}
\quad (A2)
$$

where R_n are the resistances. Through eliminating V_n, Eqs. (A1) and (A2) can be combined as

$$
\begin{pmatrix}
-iL_1\omega + \dfrac{iR_1}{-i + C_1 R_1 \omega} & -iM\omega \\
-iM\omega & -iL_2\omega + \dfrac{iR_2}{-i + C_2 R_2 \omega}
\end{pmatrix}
$$
$$
\times \begin{pmatrix} I_{L,1} \\ I_{L,2} \end{pmatrix} = 0. \quad (A3)
$$

The eigenfrequencies can be obtained by solving the characteristic equation of the matrix in Eq. (A3). By defining the normalized oscillation amplitude $a_n = I_{L,n}\sqrt{L_n/2}$, the resonant frequencies $\omega_n = 1/\sqrt{L_n C_n}$, the loss rates $\gamma_n = 1/(2R_n C_n)$, and the coupling coefficient $k = M/\sqrt{L_1 L_2}$, Eq. (A3) can be written as

$$
\begin{pmatrix}
\dfrac{-2i\gamma_1\omega + \omega^2 - \omega_1^2}{4\gamma_1 + 2i\omega} & \dfrac{-ik\omega}{2} \\
\dfrac{-ik\omega}{2} & \dfrac{-2i\gamma_2\omega + \omega^2 - \omega_2^2}{4\gamma_2 + 2i\omega}
\end{pmatrix}
\begin{pmatrix} a_1 \\ a_2 \end{pmatrix} = 0.
$$
$$(A4)$$

With the approximation $k \ll 1$ and $\gamma_n \ll \omega_n$, we have $\omega(\omega_n^2/\omega^2 - 1)/2 \approx \omega_n - \omega$. Equation (A4) then reduces to

$$
\begin{pmatrix}
i(\omega_1 - \omega) - \gamma_1 & -i\kappa \\
-i\kappa & i(\omega_2 - \omega) - \gamma_2
\end{pmatrix}
\begin{pmatrix} a_1 \\ a_2 \end{pmatrix} = 0, \quad (A5)
$$

where $\kappa = k\omega/2$ refers to the coupling rate. Equation (A5) can be recovered to the coupled-mode equations in Eq. (2) by the time-harmonic oscillation $a_n(t) \to a_n e^{i\omega t}$.

[1] S. N. Khaderi, M. G. H. M. Baltussen, P. D. Anderson, D. Ioan, J. M. J. den Toonder, and P. R. Onck, Nature-inspired microfluidic propulsion using magnetic actuation, Phys. Rev. E **79**, 046304 (2009).

[2] J. Li, X. Li, T. Luo, R. Wang, C. Liu, S. Chen, D. Li, J. Yue, S. H. Cheng, and D. Sun, Development of a magnetic microrobot for carrying and delivering targeted cells, Sci. Robot. **3**, 1 (2018).

[3] S. Palagi and P. Fischer, Bioinspired microrobots, Nat. Rev. Mater. **3**, 113 (2018).

[4] A. Cobo, R. Sheybani, H. Tu, and E. Meng, A wireless implantable micropump for chronic drug infusion against cancer, Sens. Actuator A Phys. **239**, 18 (2016).

[5] V. R. Jayaneththi, K. Aw, M. Sharma, J. Wen, D. Svirskis, and A. J. McDaid, Controlled transdermal drug delivery using a wireless magnetic microneedle patch: Preclinical device development, Sens. Actuators B Chem. **297**, 126708 (2019).

[6] Z. Wu, J. Troll, H. H. Jeong, Q. Wei, M. Stang, F. Ziemssen, Z. Wang, M. Dong, S. Schnichels, T. Qiu, and P. Fischer, A swarm of slippery micropropellers penetrates the vitreous body of the eye, Sci. Adv. **4**, eaat4388 (2018).

[7] J. Park, C. Jin, S. Lee, J. Y. Kim, and H. Choi, Magnetically actuated degradable microrobots for actively controlled

drug release and hyperthermia therapy, Adv. Healthc. Mater. **8,** 1 (2019).

[8] M. Boyvat, J. S. Koh, and R. J. Wood, Addressable wireless actuation for multijoint folding robots and devices, Sci. Robot. **2,** 1 (2017).

[9] K. A. Baldwin, J. B. De Fouchier, P. S. Atkinson, R. J. Hill, M. R. Swift, and D. J. Fairhurst, Magnetic Levitation Stabilized by Streaming Fluid Flows, Phys. Rev. Lett. **121,** 64502 (2018).

[10] D. Kim, K. Hwang, J. Park, H. H. Park, and S. Ahn, Miniaturization of implantable micro-robot propulsion using a wireless power transfer system, Micromachines **8,** 1 (2017).

[11] S. Mohith, P. N. Karanth, and S. M. Kulkarni, Recent trends in mechanical micropumps and their applications: A review, Mechatronics **60,** 34 (2019).

[12] D. Kim, M. Kim, J. Yoo, H. H. Park, and S. Ahn, Magnetic resonant wireless power transfer for propulsion of implantable micro-robot, J. Appl. Phys. **117,** 17E712 (2015).

[13] D. Kim, J. Park, H. H. Park, and S. Ahn, Generation of magnetic propulsion force and torque for microrobot using wireless power transfer coil, IEEE Trans. Magn. **51,** 1 (2015).

[14] D. Kim, J. Park, B. Park, and S. Ahn, in *Proceedings of the 2018 IEEE 7th Asia-Pacific Conference on Antennas and Propagation, APCAP 2018* (IEEE, 2018), p. 410.

[15] A. Kurs, A. Karalis, R. Moffatt, J. D. Joannopoulos, P. Fisher, and M. Soljačić, Wireless power transfer via strongly coupled magnetic resonances, Science **317,** 83 (2007).

[16] A. P. Sample, D. A. Meyer, and J. R. Smith, Analysis, experimental results, and range adaptation of magnetically coupled resonators for wireless power transfer, IEEE Trans. Ind. Electron. **58,** 544 (2011).

[17] J. Wiersig, Sensors operating at exceptional points: General theory, Phys. Rev. A **93,** 33809 (2016).

[18] C. M. Bender and S. Boettcher, Real Spectra in Non-Hermitian Hamiltonians Having PT-Symmetry, Phys. Rev. Lett. **80,** 5243 (1998).

[19] W. Chen, A. K. Özdemir, G. Zhao, J. Wiersig, and L. Yang, Exceptional points enhance sensing in an optical microcavity, Nature **548,** 192 (2017).

[20] H. Hodaei, A. U. Hassan, S. Wittek, H. Garcia-Gracia, R. El-Ganainy, D. N. Christodoulides, and M. Khajavikhan, Enhanced sensitivity at higher-order exceptional points, Nature **548,** 187 (2017).

[21] J. Doppler, A. A. Mailybaev, J. Böhm, U. Kuhl, A. Girschik, F. Libisch, T. J. Milburn, P. Rabl, N. Moiseyev, and S. Rotter, Dynamically encircling an exceptional point for asymmetric mode switching, Nature **537,** 76 (2016).

[22] Z. Dong, Z. Li, F. Yang, C. W. Qiu, and J. S. Ho, Sensitive readout of implantable microsensors using a wireless system locked to an exceptional point, Nat. Electron. **2,** 335 (2019).

[23] A. U. Hassan, B. Zhen, M. Soljačić, M. Khajavikhan, and D. N. Christodoulides, Dynamically Encircling Exceptional Points: Exact Evolution and Polarization State Conversion, Phys. Rev. Lett. **118,** 1 (2017).

[24] P.-Y. Chen, M. Sakhdari, M. Hajizadegan, Q. Cui, M. M.-C. Cheng, R. El-Ganainy, and A. Alu, Generalized parity–time

symmetry condition for enhanced sensor telemetry, Nat. Electron. **1,** 1 (2018).

[25] X. L. Zhang, S. Wang, B. Hou, and C. T. Chan, Dynamically Encircling Exceptional Points: In Situ Control of Encircling Loops and the Role of the Starting Point, Phys. Rev. X **8,** 21066 (2018).

[26] J. Schindler, A. Li, M. C. Zheng, F. M. Ellis, and T. Kottos, Experimental study of active LRC circuits with PT symmetries, Phys. Rev. A **84,** 1 (2011).

[27] S. Assawaworrarit, X. Yu, and S. Fan, Robust wireless power transfer using a nonlinear parity–time-symmetric circuit, Nature **546,** 387 (2017).

[28] Y. Ra'di, B. Chowkwale, C. Valagiannopoulos, F. Liu, A. Alu, C. R. Simovski, and S. A. Tretyakov, On-site wireless power generation, IEEE Trans. Antennas Propag. **66,** 4260 (2018).

[29] S. Assawaworrarit and S. Fan, Robust and efficient wireless power transfer using a switch-mode implementation of a nonlinear parity–time symmetric circuit, Nat. Electron. **3,** 273 (2020).

[30] M. Sakhdari, M. Hajizadegan, and P.-Y. Chen, Robust extended-range wireless power transfer using a higher-order PT-symmetric platform, Phys. Rev. Res. **2,** 013152 (2020).

[31] S. I. Babic and C. Akyel, Magnetic force calculation between thin coaxial circular coils in air, IEEE Trans. Magn. **44,** 445 (2008).

[32] C. Zeng, Y. Sun, G. Li, Y. Li, H. Jiang, Y. Yang, and H. Chen, High-Order Parity-Time Symmetric Model for Stable Three-Coil Wireless Power Transfer, Phys. Rev. Appl. **13,** 034054 (2020).

[33] H. A. Haus, *Waves and Fields in Optoelectronics* (Prentice-Hall, New Jersey, 1984).

[34] See Supplemental Material at http://link.aps.org/supplemental/10.1103/PhysRevApplied.15.024023 for derivation of the system oscillation frequencies and generalization to higher-order systems.

[35] V. V. Konotop, J. Yang, and D. A. Zezyulin, Nonlinear waves in PT -symmetric systems, Rev. Mod. Phys. **88,** 1 (2016).

[36] O. Lux, S. Sarang, O. Kitzler, D. J. Spence, and R. P. Mildren, Intrinsically stable high-power single longitudinal mode laser using spatial hole burning free gain, Optica **3,** 876 (2016).

[37] B. Levush and T. M. Antonsen, Mode competition and control in high-power gyrotron oscillators, IEEE Trans. Plasma Sci. **18,** 260 (1990).

[38] N. C. Chen, C. F. Yu, C. P. Yuan, and T. H. Chang, A mode-selective circuit for TE01 gyrotron backward-wave oscillator with wide-tuning range, Appl. Phys. Lett. **94,** 28 (2009).

[39] M. Sargent III, Theory of a multimode quasiequilibrium semiconductor laser, Phys. Rev. A **48,** 717 (1993).

[40] M. Yamada and Y. Suematsu, Analysis of gain suppression in undoped injection lasers, J. Appl. Phys. **52,** 2653 (1981).

[41] S. Longhi and L. Feng, Unidirectional lasing in semiconductor microring lasers at an exceptional point [Invited], Photon. Res. **5,** B1 (2017).

[42] Y. Zhiyenbayev, Y. Kominis, C. Valagiannopoulos, V. Kovanis, and A. Bountis, Enhanced stability, bistability,

and exceptional points in saturable active photonic couplers, Phys. Rev. A **100**, 43834 (2019).

[43] H. Wang, S. Assawaworrarit, and S. Fan, Dynamics for encircling an exceptional point in a nonlinear non-Hermitian system, Opt. Lett. **44**, 638 (2019).

[44] Z. Xiao, H. Li, T. Kottos, and A. Alù, Enhanced Sensing and Nondegraded Thermal Noise Performance Based on $\mathcal{PT}$-Symmetric Electronic Circuits with a Sixth-Order Exceptional Point, Phys. Rev. Lett. **123**, 213901 (2019).

[45] M. Farhat, M. Yang, Z. Ye, and P.-Y. Chen, Pt-symmetric absorber-laser enables electromagnetic sensors

with unprecedented sensitivity, ACS Photonics **7**, 2080 (2020).

[46] X. Hu, K. Aggarwal, M. X. Yang, K. B. Parizi, X. Xu, D. Akin, A. S. Poon, and H.-S. P. Wong, Micrometer-Scale Magnetic-Resonance-Coupled Radio-Frequency Identification and Transceivers for Wireless Sensors in Cells, Phys. Rev. Appl. **8**, 014031 (2017).

[47] A. Azizi, C. C. Tremblay, K. Gagné, and S. Martel, Using the fringe field of a clinical MRI scanner enables robotic navigation of tethered instruments in deeper vascular regions, Sci. Robot. **4**, 1 (2019).